Flare location on the solar disk: Modeling the thermosphere and ionosphere response

Liying Qian,[1] Alan G. Burns,[1] Phillip C. Chamberlin,[2] and Stanley C. Solomon[1]

Received 21 December 2009; revised 24 February 2010; accepted 1 April 2010; published 14 September 2010.

[1] Solar flare enhancements to the soft X-ray (XUV) and extreme ultraviolet (EUV) spectral irradiance depend on the location of the flare on the solar disk. Most emission lines in the XUV region (~0.1 to ~25 nm) are optically thin and are weakly dependent on the location of the flare, but in the EUV region (~25 to ~120 nm), many important lines and continua are optically thick, so enhancements are relatively smaller for flares located near the solar limb, due to absorption by the solar atmosphere. The flare irradiance spectral model (FISM) was used to illustrate these location effects, assuming two X17 flares that are identical except that one occurs near disk center and the other near the limb. FISM spectra of these two flares were used as solar input to the National Center for Atmospheric Research (NCAR) thermosphere-ionosphere-mesosphere electrodynamics general circulation model (TIME-GCM) to investigate the ionosphere/thermosphere (I/T) response. Model simulations showed that in the *E* region ionosphere, where XUV dominates ionization, flare location does not affect I/T response. However, flare-driven changes in the *F* region ionosphere, total electron content (TEC), and neutral density in the upper thermosphere, are 2–3 times stronger for a disk-center flare than for a limb flare, due to the importance of EUV enhancement. Flare location did not affect the timing of the ionospheric response, but the thermospheric response was ~20 min faster for the disk-center flare. Model simulations of I/T responses to an X17 flare on 28 October 2003 were consistent with measurements of TEC and neutral density changes.

Citation: Qian, L., A. G. Burns, P. C. Chamberlin, and S. C. Solomon (2010), Flare location on the solar disk: Modeling the thermosphere and ionosphere response, *J. Geophys. Res.*, *115*, A09311, doi:10.1029/2009JA015225.

1. Introduction

[2] Enhanced spectral emissions from solar flares take place throughout the solar atmosphere and produce rapid increases of X-ray (factors of 10–100) and extreme ultraviolet (EUV) (factors of 2–10) radiation. This rapid increase of X-ray and EUV irradiance enhances ionization in the upper atmosphere. Ionospheric effects of solar flares, or sudden ionospheric disturbances (SIDs), have been studied since 1960s due to their effects on radio communications and navigation systems. The SID phenomena, such as short wave fadeout, sudden phase anomaly, sudden frequency deviation, and sudden increase of TEC, were investigated using Doppler sounding systems in the 1960s and 1970s [*Mitra*, 1974; *Davies*, 1990]. *Mendillo et al.* [1974] constructed the first synoptic picture of ionospheric total electron content (TEC) response to a large solar flare. More recently, real-time, high-temporal resolution (~1 min) TEC measurements by the ground-based GPS network have been collected to form global TEC maps [e.g., *Rideout and Coster*, 2006; *Coster and Komjathy*, 2008]. Studies of terrestrial effects of solar flares have recently extended to the neutral atmosphere. Neutral density changes have been obtained from accelerometer measurements of nongravitational accelerations on the CHAMP satellite [*Reigber et al.*, 2002; *Sutton et al.*, 2005, 2006].

[3] These observations of I/T responses to solar flares have indicated that changes of neutral density and TEC do not scale directly to the intensity of solar flares as classified by their X-ray brightness. GPS observations indicated that the mean amplitude of the TEC responses to flares depended on the flare locations on the Sun [*Zhang et al.*, 2002; *Afraimovich et al.*, 2002; *Tsurutani et al.*, 2005; *Liu et al.*, 2006]. *Tsurutani et al.* [2006] compared GPS measurements of the 28 October 2003 (X17) and 4 November 2003 (X28) solar flares; the X17 flare located near the center of the solar disk, whereas the X28 flare was at the limb. As a result, the TEC increase during the X17 flare was ~5 times the TEC increase during the X28 flare. They concluded that TEC response does not scale to EUV flare amplitude and that this phenomenon cannot be easily understood without fully modeling the detailed physics and chemistry of the terrestrial effects of solar flares.

[1]High-Altitude Observatory, National Center for Atmospheric Research, Boulder, Colorado, USA.
[2]Solar Physics Laboratory, NASA Goddard Space Flight Center, Greenbelt, Maryland, USA.

Copyright 2010 by the American Geophysical Union.
0148-0227/10/2009JA015225

[4] Effects of flare location on the optically thin XUV are very different from those on most of the more optically thick EUV that is formed lower in the solar atmosphere [*Chamberlin et al.*, 2008]. Understanding these effects on I/T responses to flares is critical, since solar flares have significant effects on satellite drag, radio communications, and GPS navigation accuracy. Previous modeling studies using ionospheric modeling [e.g., *Meier et al.*, 2002; *Huba et al.*, 2005, *Strickland et al.*, 2007] and including neutral atmosphere coupling [e.g., *Woods et al.*, 2008] were limited by the partial coverage of the solar spectra in the X-ray and EUV wavelengths and the lack of temporal resolution for the flare irradiance enhancement. In this paper, we employ a solar flare model, the flare irradiance spectral model [*Chamberlin et al.*, 2008] to produce two flare spectra that differed only in their location on the solar disk. These spectra showed how flare locations affect the intensity of sudden increases of irradiance in the XUV, EUV, and FUV (120–195 nm) ranges. They were then used as solar input to the NCAR TIME-GCM [*Roble and Ridley*, 1994]. Model studies were conducted to investigate flare location effects on the I/T responses to solar flares, connections between flare location effects on a solar spectrum and on the I/T responses, and the underlying physical and chemical mechanisms that determine these effects and connections. In addition, model simulations of I/T responses to an X17 flare on 28 October 2003 were compared to CHAMP neutral density and global GPS TEC measurements to show I/T responses to the X17 near-center flare.

2. Model Description

2.1. FISM Solar Flare Model

[5] FISM [*Chamberlin et al.*, 2007, 2008] is an empirical model developed for space weather applications based on measurements from the thermosphere-ionosphere-mesosphere energetics and dynamics (TIMED) Solar EUV Experiment (SEE) [*Woods et al.*, 2005]. It estimates the solar irradiance at wavelengths from 0.1–190 nm at 1 nm resolution with a time cadence of 60 s. This is sufficient temporal resolution to model variations due to solar flares, for which few accurate measurements at these wavelengths exist. FISM provides accurate modeling of the daily component variations, including variations from the solar cycle and solar rotation from 1947 until the present. FISM also includes a flare component that estimates the solar irradiance variations from both the impulsive and gradual phases of solar flares. The flare component of FISM is available from the start of the GOES X-ray Sensor (XRS) measurements in 1974 until the present. FISM fully quantifies, on all timescales, the changes in the solar irradiance in the wavelength range directly affecting the planetary thermosphere and ionosphere.

[6] There are significant center-to-limb variations (CLVs) of active regions as they rotate around the observable solar disk [e.g., *Worden et al.*, 2001]. Likewise, TIMED/SEE observations showed that there were significant CLV effects on irradiance enhancements during solar flares, and CLV effects of the optically thin X-ray wavelengths are very different from the optically thick EUV emissions. FISM makes wavelength-dependent CLV corrections for enhanced flare emissions based on these observations from TIMED/SEE. FISM has a CLV function for each wavelength, and coefficients for these functions were obtained through data fitting of 28 (M1.0–X17.4) flares observed by TIMED/SEE from 2002–2005. These flares occurred over a wide variety of solar activity conditions, ranging from the low middle of the solar cycle to extreme solar maximum. Therefore, we may consider that the FISM CLV effects are applicable to virtually all solar activity conditions and for M and X class flares. The details of how FISM accounts for the flare CLV are given in the study of *Chamberlin et al.* [2008]. The flare location input for FISM is determined from NOAA solar event reports information that uses full disk solar images provided by the GOES solar X-ray imager. Both the longitude and the latitude are used in determining the most accurate heliocentric angle for the CLV correction in FISM [*Chamberlin et al.*, 2008].

2.2. NCAR TIME-GCM

[7] The NCAR TIME-GCM is a time dependent, 3-D model that solves the fully coupled, nonlinear, hydrodynamic, thermodynamic, and continuity equations of the neutral gas self-consistently with the ion energy, ion momentum, and ion continuity equations from the upper stratosphere to the thermosphere. It combines all previous features of the NCAR upper atmospheric general circulation models including a self-consistent, fully coupled thermosphere and ionosphere, and electrodynamics driven by the neutral wind circulation [*Roble et al.*, 1988; *Richmond et al.*, 1992; *Roble and Ridley*, 1994]. The TIME-GCM calculates global neutral winds, neutral temperatures, major and minor neutral species composition, electron and ion densities and temperatures, and the ionospheric dynamo electric field. It has a horizontal resolution of 5° × 5°. The model assumes hydrostatic equilibrium and solves equations on pressure surfaces. The pressure interfaces are defined as $\mathrm{lev} = \ln(P_0/P)$, and P_0 is a reference pressure of 5×10^{-4} μb. The vertical range of the pressure interfaces is from −17 to 7. The model has 49 pressure surfaces from ~30 to ~600 km with a vertical resolution of one half-scale height. The external forcing for the model is solar irradiance, either parameterized using the $F_{10.7}$ index or supplied by measurements [*Solomon and Qian*, 2005], auroral particle precipitation, an imposed magnetospheric electric field, and the amplitudes and phases of tides from the lower atmosphere specified by the global scale wave model [*Hagan et al.*, 1999]. Gravity wave effects are parameterized based on the linear saturation theory of *Lindzen* [1981].

3. Data

3.1. CHAMP Neutral Density

[8] The CHAMP satellite was launched into a near-circular orbit with an inclination of 87.3° on 15 July 2000 [*Reigber et al.*, 2002]. The high inclination ensures almost complete latitudinal coverage from pole to pole. Neutral density is obtained from accelerometer measurements of nongravitational accelerations on the CHAMP satellite [*Reigber et al.*, 2002] using standard methods [e.g., *Sutton et al.*, 2005, 2006]. The measured densities are normalized to a constant altitude of 400 km using NRLMSISE00 [*Picone et al.*, 2002]. CHAMP neutral density data has high temporal resolution (~30 to ~60 s) and good spatial resolution (~3° in latitude) and, thus, are suitable for flare studies. The neutral density

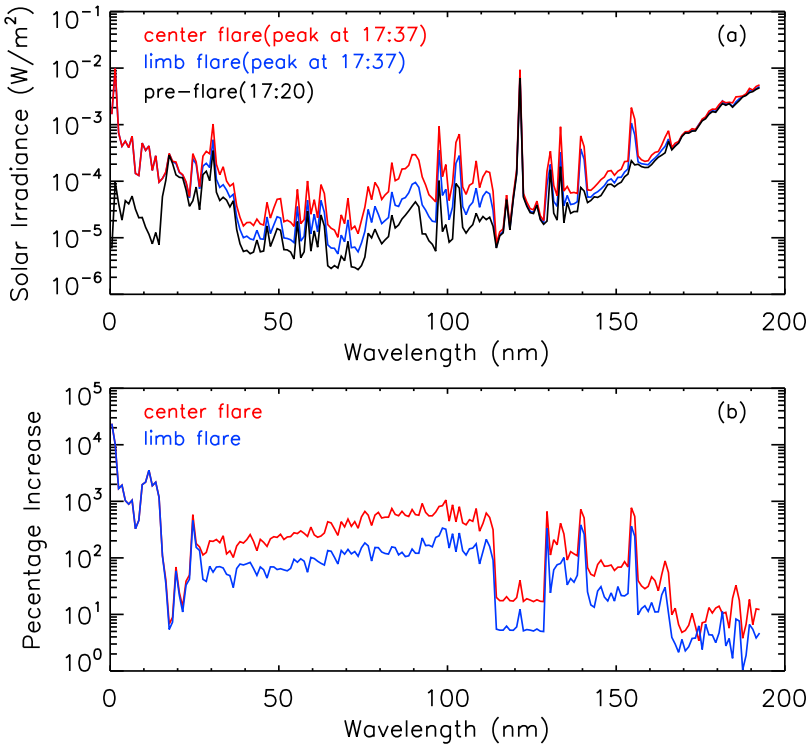

Figure 1. Enhancement of FISM solar irradiance from 0.05 to 195 nm for two identical X17 solar flares except that one occurs near the center of solar disk and the other near the limb. The flare starts at 1720 UT and reaches peak at 1737 UT. (a) Solar spectra before the flares (black), at peak for the center flare (red), and at peak for the limb flare (blue). (b) Percentage increases of solar irradiance at peaks compared to the pre-flare condition (center flare (red) and limb flare (blue)).

data from 2001018 to 2008112 are available online for public access from the University of Colorado.

3.2. TEC From Ground-Based GPS Network

[9] Ground-based TEC measurements have been available from a global network of GPS stations on a routine basis since at least 2001 [*Rideout and Coster*, 2006; *Coster and Komjathy*, 2008]. The Massachusetts Institute of Technology Automated Processing of GPS (MAPGPS) software suite [*Rideout and Coster*, 2006] has been developed to calculate TEC from the network of worldwide GPS receivers. Recently, the MAPGPS processing code was significantly enhanced to improve error handling. Errors are now tracked throughout the processing, and random and correlated errors are handled separately. This allows optimal estimation of binned measurements and allows error values to be calculated independently for each binned measurement. The bin-to-bin variability in the TEC measurements was greatly reduced using this approach. GPS TEC data from 2001 to 2007 have been processed using the updated version of MAPGPS. These TEC estimates are output in $1° \times 1°$ bins of latitude/longitude every 5 min, distributed over those locations where data are available. These data can be downloaded online from the Madrigal database at the Massachusetts Institute of Technology Haystack Observatory.

4. Flare Spectra

[10] FISM was used to simulate flare spectra at 1 nm and 1 min resolutions for two assumed X17 flare events. These two simulated flares were the same except that they occurred at different locations on the solar disk. One occurred near the disk center (1° from the center of the solar disk), and the other occurred near the limb (85° from the center). Similarly, the same constant pre-flare and post-flare conditions were assumed for these two flares in our analysis. The flares started at 1720 UT and soft X-ray peaked at 1737 UT. Figure 1a shows the pre-flare spectrum, peak limb flare spectrum, and peak center flare spectrum. Solar irradiance increased from 1 to 2 orders of magnitude in the shortest XUV range (<16 nm), up to a few times in the rest of XUV (16–27 nm) and EUV range, and reduced to a few percent in the longest FUV wavelengths. Percentage changes of solar irradiance from pre-flare to flare peak for the limb and center flares are shown in Figure 1b. In the wavelength range short of 16 nm, there was no difference in the irradiance enhancement produced by the center flare and the limb flare; between ~16 and ~27 nm, enhancement of irradiance by the center flare was a few percent stronger compared to the limb flare. Such differences became significant for wavelengths longer than 27 nm. The X17 center flare at its peak provided ~50% to ~250% more solar irradiance to the terrestrial atmosphere than the X17 limb flare did in the EUV range (27–105 nm). *Chamberlin et al.* [2008] analyzed uncertainties in FISM estimations and found that these uncertainties were below 40% for EUV wavelengths greater than 14 nm. Figure 1b showed that flare location effect in the EUV range was in the order of 200% for most of the EUV wavelengths. Therefore, flare location effect in the

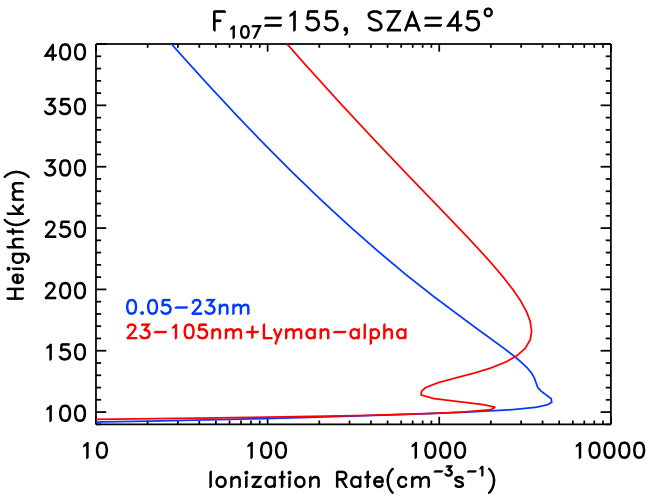

Figure 2. Profiles of ionization rates under solar medium condition ($F_{10.7} = F_{10.7a} = 155$) at solar zenith angle 45°. Solar spectrum used for this calculation was EUVAC solar proxy model, and the atmosphere was MSIS90 atmosphere. Ionization rate by wavelength range 0.05–23 nm (blue); ionization rate by wavelength range 23–105 nm and the Lyman-α (red).

EUV wavelength range is significant compared to the FISM uncertainties. This percentage differences in EUV enhancement (CLV effects) will determine the model-simulated, percentage differences in I/T responses to the center flare and the limb flare. Therefore, uncertainties in FISM estimations of the CLV effects will propagate proportionally to the simulated percentage differences in I/T responses. As we mentioned earlier, the CLV effects were obtained based on flares that occurred over a wide variety of solar activity conditions, ranging from the low middle of the solar cycle to extreme solar maximum [*Chamberlin et al.*, 2008], with intensities ranging from M1.0 to X17.4, we may consider that the FISM CLV effects are applicable to virtually all solar activity conditions and for M and X class flares. FISM estimations of the CLV effects have been confirmed by comparing FISM with observations of two flares by the Solar and Heliospheric Observatory solar extreme ultraviolet monitor. One flare was located near the disk center (28 October 2003 at 18°) and the other near the disk limb (4 November 2003 at 85°) [*Chamberlin et al.*, 2008].

[11] The two simulated FISM X17 flare spectra were used as solar input to the TIME-GCM to investigate how flare locations influence the I/T responses to solar flares and the physical and chemical mechanisms that drive the responses. In addition, FISM flare spectra for an X17 near-center flare that occurred on 28 October 2003 were used as solar input to the TIME-GCM to compare model-simulated I/T responses to CHAMP neutral density and ground-based TEC measurements.

5. Results

5.1. Vertical Distribution

[12] The most important feature shown in Figure 1 is that XUV increases for the center flare and the limb flare were nearly identical, but solar irradiance increases in the EUV was significantly larger for the center flare compared to the limb flare. XUV and EUV ionize the thermosphere in different altitude regions; this can be demonstrated using altitude profiles of ionization rates by XUV and EUV radiation. Photoionization rates given by Chapman function [*Banks and Kockarts*, 1973] were calculated using an MSIS90 [*Hedin*, 1987, 1991] atmosphere (O, O_2, and N_2 density) and EUV flux model for aeronomic calculations (EUVAC) [*Richards et al.*, 1994] solar flux, under solar medium conditions ($F_{10.7} = F_{10.7a} = 155$) and at solar zenith angle 45°. Figure 2 shows the ionization rates by solar irradiance in the wavelength ranges of 0.05–23 nm and 23–105 nm together with the Lyman-α (121.56 nm). XUV ionization peaks in the E region, whereas EUV dominates ionization above 150 km. The EUV ionization profile has a second peak in the E region; this is ionization by the Lyman-β (102.57 nm). Given this knowledge about the ionization, we will now examine the altitude distribution of flare location effects on I/T responses.

[13] Figure 3 shows TIME-GCM simulated ion production rate, ion loss rate, and electron density profiles for pre-flare condition, at limb flare peak, and at center flare peak (top frames), respectively. The bottom frames of Figure 3 show the percentage increases of neutral temperature, neutral composition, and neutral density from pre-flare to flare peaks. These frames show conditions in the equatorial region (2.5°) at local noon. Ionospheric responses to solar flares were strongest in the E region, yet electron density in the region was small as shown in the top frames of Figure 3. Therefore, profiles of the ionospheric parameters are shown in the altitude range from 90 to 200 km to show the E region features.

[14] The top frames of Figure 3 show that the enhancement of ion production, ion loss, and electron density due to the limb flare was nearly identical to those due to the center flare. Some small differences of electron density near the E region peak were, however, visible, most likely due to ionization by the Lyman-β (Figure 2). Flare location effects on the enhancement of these three parameters diverge above ~120 km, with more enhanced production rate, loss rate, and electron density for the center flare compared to the limb flare. Since electron density in the F region is the main contributor to TEC, the center flare should have caused more enhanced TEC than the limb flare did.

[15] Thermospheric responses to solar flares were very small in the lowest part of the thermosphere, and there were no flare location effects in this altitude region; both flare responses and flare location effects increased significantly with altitude (Figure 3, bottom frames). This is because neutral gas heating by solar irradiance dominates in the 150–300 km altitude range [*Roble*, 1995], the region where EUV is the main source of ionization, and the center flare had 50%~250% more enhanced EUV than the limb flare.

[16] In the lower thermosphere, NO is excited through collisions with neutral constituents (mainly atomic oxygen). The excited NO radiates in the infrared and cools the thermosphere. NO infrared cooling at 5.3 μm is considered to be a thermosphere thermostat and plays important role in the thermosphere energy budget. NO is mainly produced by reactions between excited atomic nitrogen N(^4S) and N(^2D) with O_2. XUV irradiance has high energy, allowing it to

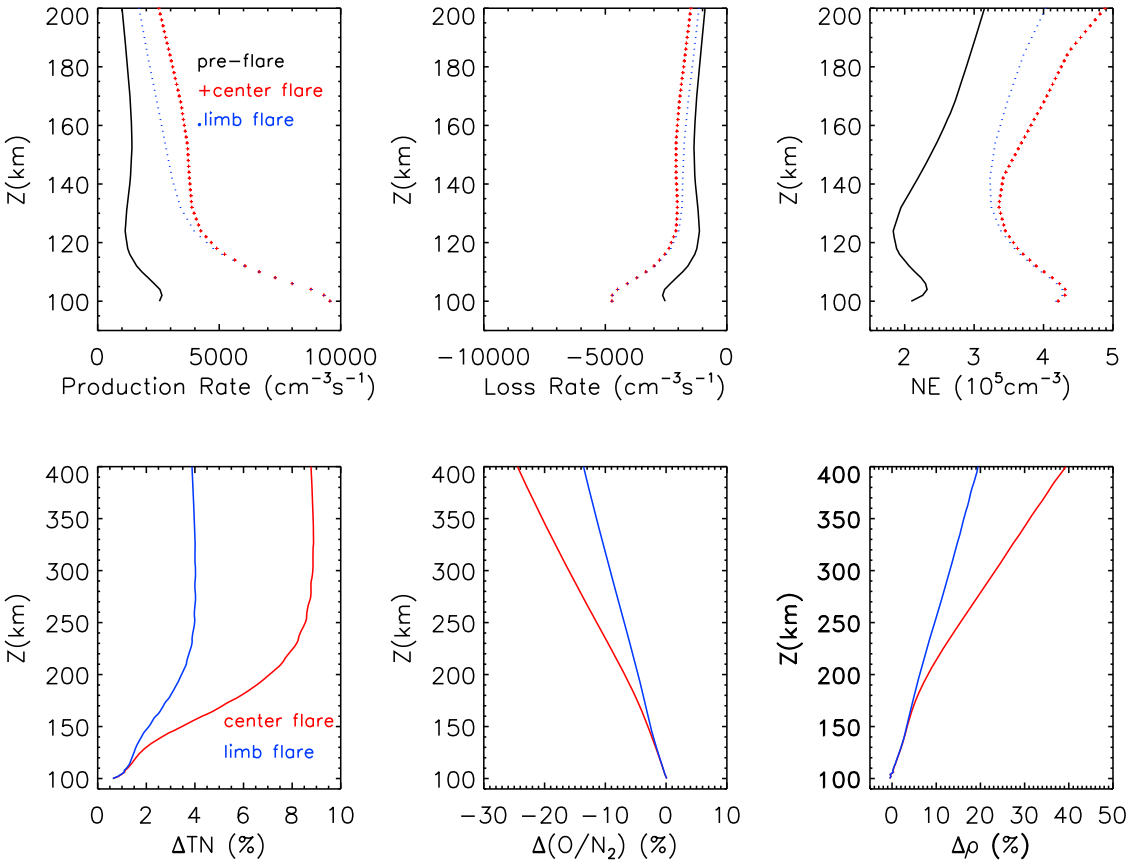

Figure 3. TIME-GCM simulated I/T responses to the X17 limb flare and X17 center flare in the equatorial region (2.5°) at local noon. (top frames) Ion production rates, ion loss rates, and electron density profiles under pre-flare condition (black), at flare peak of the X17center flare (red), and at flare peak of the X17 limb flare (blue). (bottom frames) Percentage increases of neutral temperature, O/N_2, and neutral density from pre-flare condition to flare peaks (center flare (red) and limb flare (blue)). FISM solar spectra were used as solar input for the TIME-GCM.

break the strong N_2 molecular bond and consequently to produce excited atomic nitrogen atoms. XUV increases significantly during solar flares. Therefore, NO cooling may have a strong solar flare response, which, in turn may play an important role in determining how the thermosphere responds to, and recovers from, solar flares. Thus, it is important to understand how flare location affects NO cooling responses.

[17] Figure 4a shows NO density profiles at pre-flare, center-flare peak, and limb-flare peak at local noon in the equatorial region (2.5°). Peak NO density nearly doubled at the flare peaks. Since NO is produced by XUV and there is nearly no difference in XUV enhancement for the center flare and the limb flare, NO enhancement was largely identical for the center flare and the limb flare. Therefore, flare location did not affect NO enhancement. Figure 4b shows corresponding profiles of NO cooling rates per unit volume. NO cooling increased nearly 60% at flare peak. This indicates that NO cooling enhancements during the flares were significant. It should act as thermostat for solar flare events as well. Enhancement of NO cooling rates was the same at lower altitudes (below 120 km) for the center flare and the limb flare. Above 120 km, enhancement of NO cooling became slightly larger for the center flare. This difference was evident when the cooling rate was calculated per unit mass as shown in Figure 4c. *Mlynczak et al.* [2005] suggested that NO cooling enhancement during solar storms is mainly determined by NO density as well as temperature. Since NO enhancement was nearly same for the center flare and the limb flare, the larger NO cooling per unit mass is likely due to larger temperature increases for the center flare compared to the limb flare (Figure 3). Differences in NO cooling rates per unit mass at their peaks (~170 km) were about 15%. This difference in NO cooling enhancement due to flare location may, to some degree, reduce flare location effects on thermospheric responses, specifically, the temperature and neutral density responses in the middle thermosphere (Figure 3), since more heating was partially compensated for by more cooling for the center flare.

5.2. Variations With Time

[18] Section 5.1 showed that thermospheric responses to solar flares mainly occur in the upper thermosphere, and flare locations had a large effect on these responses. Figure 5 compares neutral temperature and neutral density disturbances at 400 km due to the simulated X17 center and limb flares at local noon. Enhancement of neutral temperature and density due to solar flares occurred at all latitudes;

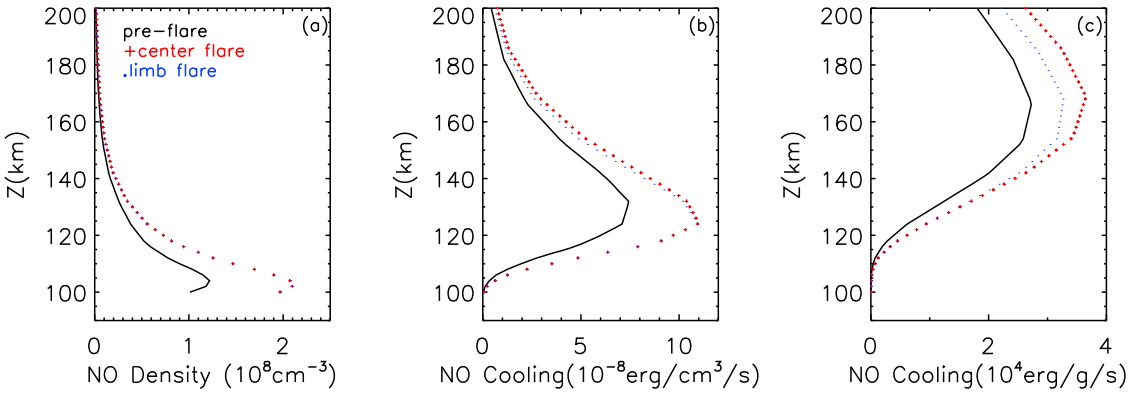

Figure 4. TIME-GCM simulated NO density and NO cooling responses to the X17 limb flare and X17 center flare in the equatorial region (2.5°) at local noon. (a) NO density, (b) NO cooling rate per unit volume, and (c) NO cooling rate per unit mass (pre-flare (black), at flare peak of the X17center flare (red), and at flare peak of the X17 center flare (blue)). FISM solar spectra were used as solar input for the TIME-GCM.

flare location effects were also seen at all latitudes. At 400 km, maximum increases of neutral temperature for the center flare and the limb flare were ~85 and ~30 K, respectively, and the corresponding neutral density increases were ~20% and ~10%, respectively. Neutral temperature and neutral density reached their peak ~1.5 h after the flare peak. Flare locations affected this timing of peak responses; peak responses of neutral temperature and neutral density to

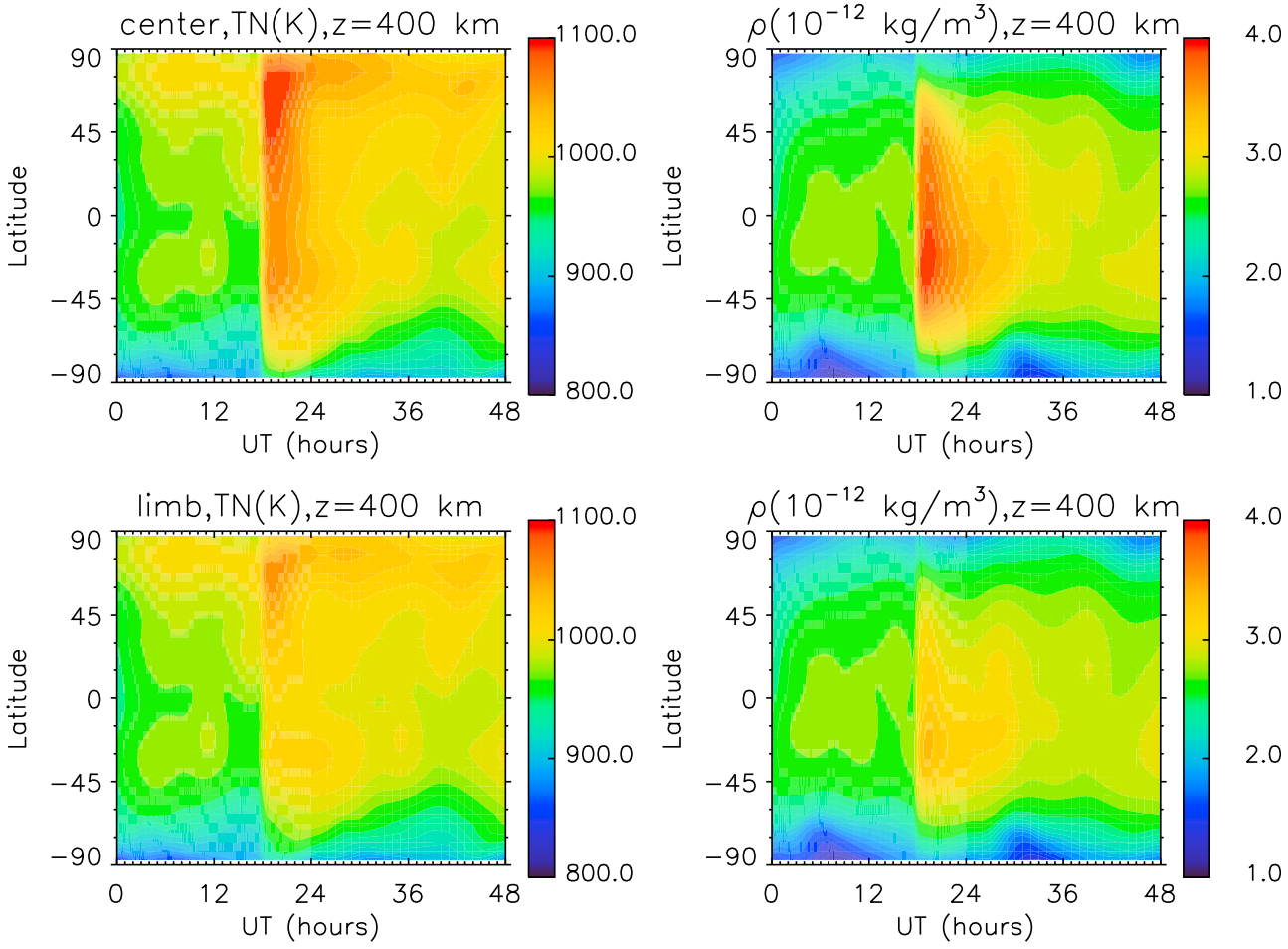

Figure 5. Comparisons of neutral temperature and neutral density enhancement at 400 km at local noon simulated by the TIME-GCM. FISM solar spectra were used as solar input for the TIME-GCM. (top) Center flare and (bottom) limb flare.

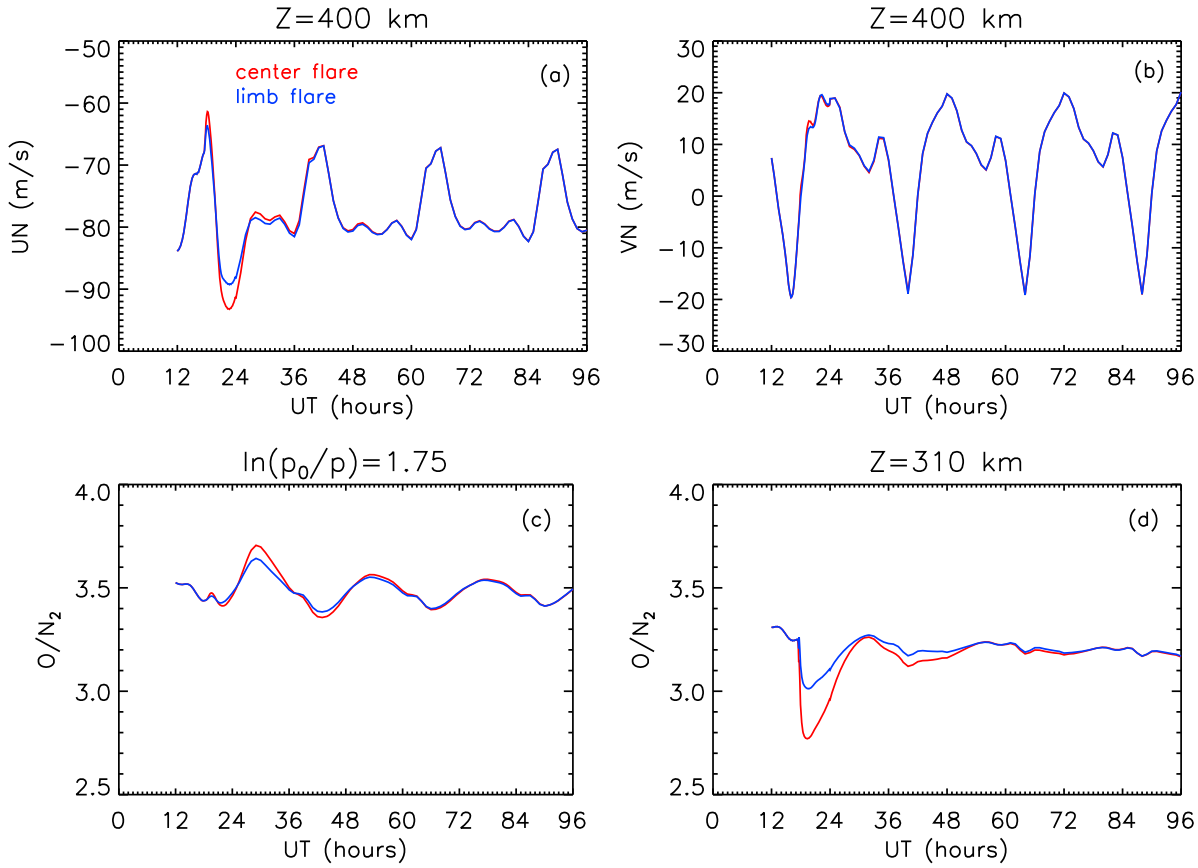

Figure 6. Variations of (a) zonal wind at 400 km, (b) meridional wind at 400 km, (c) O/N_2 at constant pressure surface lev = $\ln(P_0/P)$ = 1.75, and (d) O/N_2 at 310 km, from pre-flare, through flare peak, to 3 days after the flares, simulated by the TIME-GCM in the equatorial region (2.5°) at local noon. FISM solar spectra were used as solar input for the TIME-GCM (center flare (red) and limb flare (blue)).

the limb flare occurred ~20 min later than those to the center flare.

[19] Figure 6 shows variations of zonal wind at 400 km, meridional wind at 400 km, O/N_2 at a fixed pressure surface (lev = $\ln(P_0/P)$ = 1.75) near the F_2 peak, and O/N_2 at 310 km from pre-flare, through flare peak, to 3 days after the flares due to the X17 center flare and the X17 limb flare in the equatorial region (2.5°N) at local noon. A height of 310 km was chosen to show O/N_2 at a fixed altitude since O/N_2 at this altitude had a similar magnitude compared to O/N_2 at the constant pressure surface lev = 1.75. Since time series of variables at fixed geographic latitude and fixed local time include longitudinal variations of these variables, the time series were extended 3 days after the solar flares to differentiate variations due to solar flares from variations due to longitude. Heating due to solar flares set up a pressure gradient. In the equatorial region, such enhancement of pressure gradient was mainly in the zonal (day-night) direction and negligible in the meridional direction since there was significant enhancement of zonal wind but very small changes in the meridional winds (Figures 6a and 6b). Zonal wind peaked ~2.5 h after neutral temperature and neutral density reached their peaks.

[20] Both the neutral temperature disturbances and neutral wind disturbances can cause composition disturbances. The composition disturbances due to these two causes can be differentiated by their characteristics. O/N_2 change due to expansion as a result of heating occurred nearly simultaneously with temperature increase. This composition change was negligible on a constant pressure surface (Figure 6c) but was clearly shown at a fixed altitude (Figure 6d). However, neutral wind disturbances caused much delayed composition disturbances on a constant pressure surface that maximized ~10 h after the flare peak (Figure 6c), and this composition disturbance was relatively weak compared to the disturbance at fixed altitude due to expansion.

[21] Ionospheric responses to solar flares and their CLV effects are shown in Figure 7. Figure 7 compares time variations of ratios of electron density, ion production, and ion loss to their pre-flare (1720 UT) values for the center flare and the limb flare in the equatorial region at local noon. Enhancement of ion production, ion loss, and electron density were the same for the center flare and the limb flare in the E region below pressure surface ~−3. Effects of flare location occurred in the F region above this pressure surface; near the F_2 peak, maximum increases of electron density due to the center flare and the limb flare were ~50% and ~15%, respectively.

[22] Ionospheric responses to solar flares were nearly instant; the ion production rate responded to sudden increases of solar XUV and EUV radiation instantly and reached a peak only ~3 min after the flare peak; ion loss

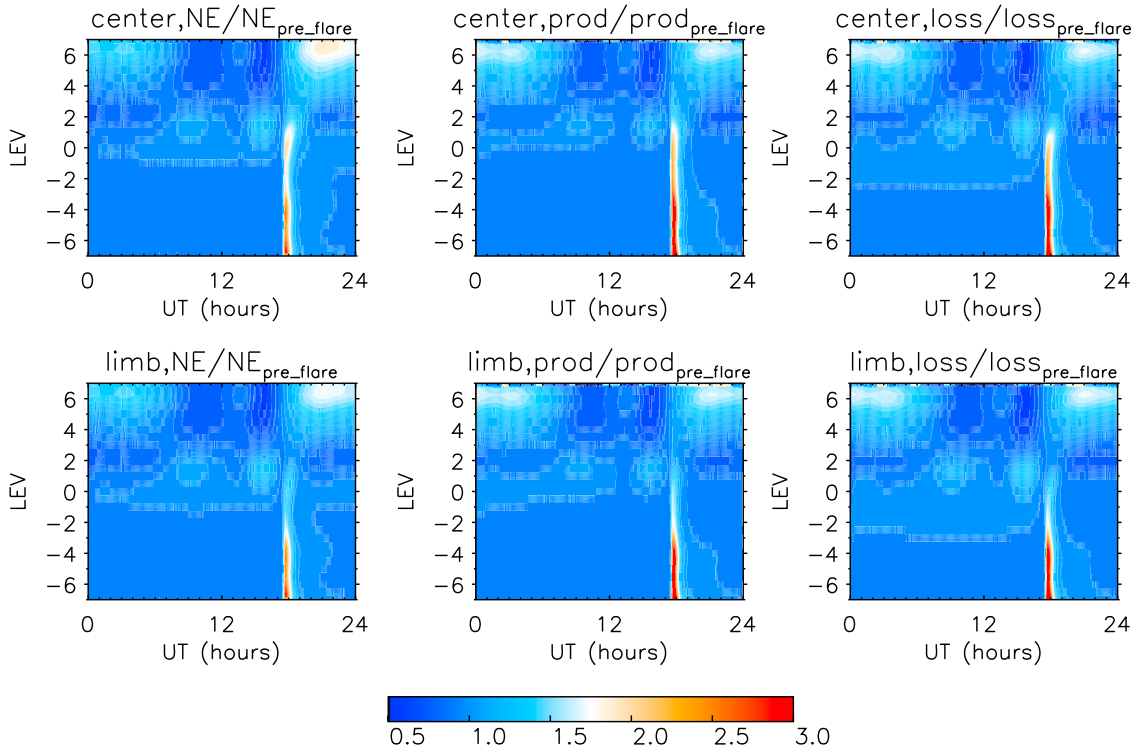

Figure 7. Comparisons of ratios of peak electron density, peak ion production, and peak ion loss to their pre-flare values on pressure surfaces-UT cross section, in the equatorial region (2.5°) at local noon, simulated by the TIME-GCM. lev = ln(P_0/P), where P_0 is a reference pressure of 5×10^{-4} μb. FISM solar spectra were used as solar input for the TIME-GCM. (top) Center flare and (bottom) limb flare.

processes reacted immediately to the increased production and reached a peak ~20 min later. Model simulations showed that these responses of ion production and loss to increased XUV and EUV were the main causes of electron density enhancement during solar flares. The responses of ion transport processes to solar flares, including ambi-polar diffusion, ion transport by neutral wind, ion transport due to E × B drift, were relatively small compared to ion production and loss effects. The peak electron density enhancement occurred ~30 min after the flare peak. Model simulations also showed that flare locations did not affect the timing of peak responses of the ionospheric parameters. In addition to this large near-instant enhancement, both production and loss disturbance had some small disturbances that lagged ~2 days after the solar flares. These small disturbances were feedback from disturbances of the neutral temperature (Figure 5) and composition (Figure 6c). Thermospheric disturbances responded and recovered much slower than the ionospheric disturbances and caused some feedback disturbance to the ionosphere that was very small compared to disturbances due to the direct responses of the ionosphere to sudden increases of XUV and EUV; they are not evident in Figure 7. Figure 7 demonstrates a cause-effect relation between ion production/loss disturbances and electron density disturbances during solar flares.

5.3. Simulations and Observations of a Centrally Located Flare

[23] An X17 flare occurred near the center of the solar disk, at 18° off disk center, on 28 October 2003. It started ~0950 UT, underwent the most significant and fastest increase of irradiance from ~1100 to 1110 UT, and reached a peak at ~1110 UT. FISM flare spectra for this X17 flare were used as input to the TIME-GCM. TIME-GCM simulated I/T disturbances were compared to CHAMP neutral density observations and TEC measurements made by the global ground-based GPS network. Figure 8 shows the neutral density comparison for both day and night. The CHAMP ascending node was at 0105 local time, and the descending node was at 1308 local time. Model-simulated neutral density enhancements were slightly weaker than those observed by CHAMP, and the model simulations and the data showed an increase of neutral density of 30%–40%. Neutral density enhancements on the nightside were also evident, but there was a delay of approximately 5 h compared to the dayside enhancements. This nightside disturbance was originated and transported from the dayside.

[24] Figure 9 compares a TEC map before the flare (1100 UT) with one at the flare peak (1110 UT) observed by the ground-based GPS network and simulated by the TIME-GCM. GPS observations were insufficient in terms of global coverage, but TEC enhancement was evident and the TEC maps were consistent with the model simulations. TEC difference between the flare peak and pre-flare were calculated to examine TEC enhancement during the flare. In order to remove local time variation, TEC difference between 1110 and 1100 UT from the previous day (27 October 2003) were also calculated. This TEC difference was subtracted from the corresponding TEC difference on 28 October 2003 to obtain flare-induced TEC enhancement. Model-simulated

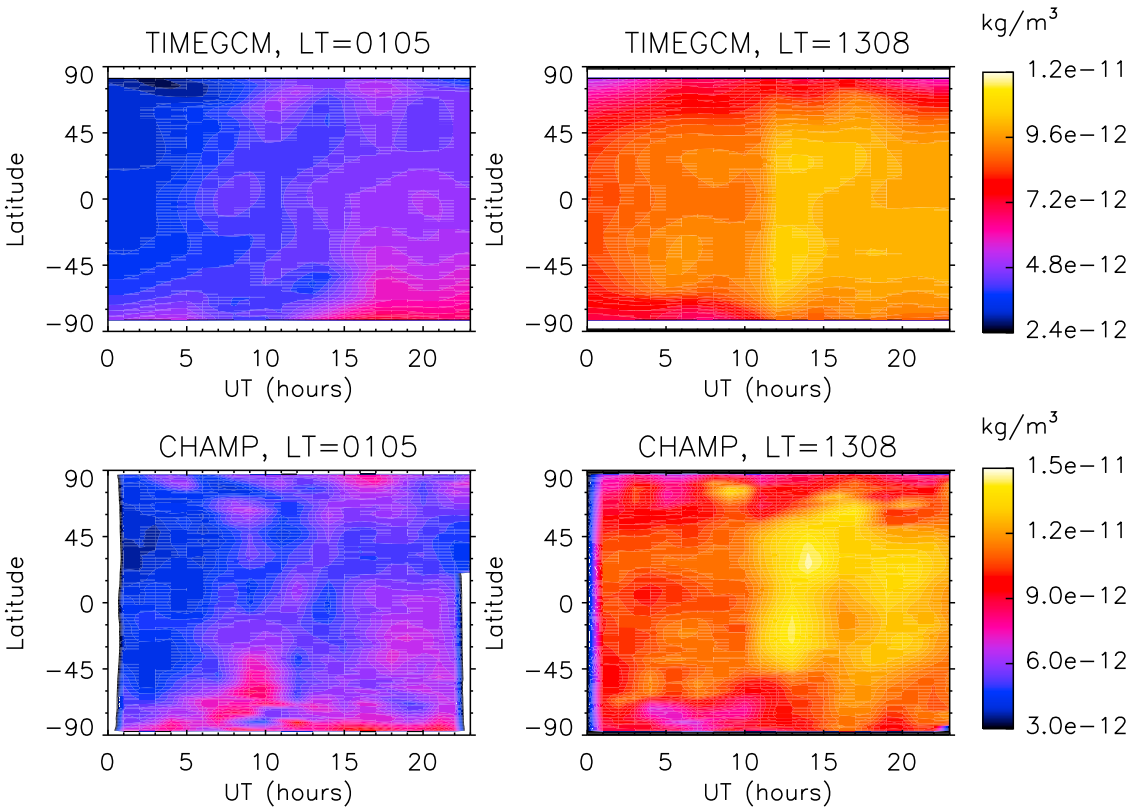

Figure 8. Comparisons of TIME-GCM simulated neutral density enhancement to CHAMP observed neutral density enhancement responding to the X17 near-center flare occurred on 28 October 2003, during (left) CHAMP ascending node (0105 LT) and (right) CHAMP descending node (1308 LT). The flare started ~0950 UT and peaked at ~1110 UT. FISM solar spectra were used as solar input for the TIME-GCM.

local time variation of TEC enhancement is consistent with the observation, but the simulated TEC enhancement is slightly weaker. The observed and simulated maximum TEC enhancement for this flare was approximately 20 TEC units and 15 TEC units, respectively.

6. Discussions and Conclusions

[25] TIMED/SEE measurements showed that effects of center-to-limb variations (CLV) of solar flares on the optically thin X-ray were very different from those on the optically thick EUV radiation. FISM was used to demonstrate this wavelength dependence of the CLV effects by assuming that two X17 flares were identical, except that one occurred near the center of the solar disk and the other near the limb. In the wavelength range short of ~16 nm, there was no difference in enhancement of solar irradiance by the center flare and the limb flare; between ~16 and ~27 nm, enhancement of irradiance caused by the center flare was a few percent more than that caused by the limb flare. Such differences were significant for wavelengths longer than 27 nm. Enhancement of EUV irradiance due to the center flare was ~50% to ~250% more compared to the limb flare.

[26] This wavelength dependence of flare location effects influenced how the terrestrial atmosphere responded to flares with different locations on the solar disk. In the *E* region, where XUV dominates ionization, percentage responses of the ionosphere to solar flares were largest, since XUV enhancements during solar flares were stronger than EUV ones. However, since flare location had little effect on XUV enhancement during solar flares, there was nearly no absolute difference in ion production, ion loss, and thus electron density enhancement between the center flare and the limb flare. The modeled neutral atmospheric responses to solar flares (temperature and density) were very small in this lowest part of the thermosphere. In addition, similarly to the ionospheric responses, the minor species NO had the largest flare responses, since NO is mainly produced by XUV, but flare location had little effect on this NO enhancement.

[27] In the *F* region where EUV is the main source of ionization, enhancements of ionospheric parameters was much larger for the center flare compared to the limb flare. The percentage increases of electron density near the F_2 peak for the center flare and the limb flare were ~50% and ~15%, respectively. Thermospheric responses (temperature and density) increased greatly with altitude and were much stronger for the center flare. This is because neutral gas heating by solar irradiance dominates in the 150–300 km, the region where EUV is the main source of ionization. In the upper thermosphere (~400 km), neutral temperature increases due to the X17 center flare and the X17 limb flare were approximately 85 and 30 K, respectively. The corresponding neutral density enhancements were around 20% and 10%, respectively. In addition, the flare location

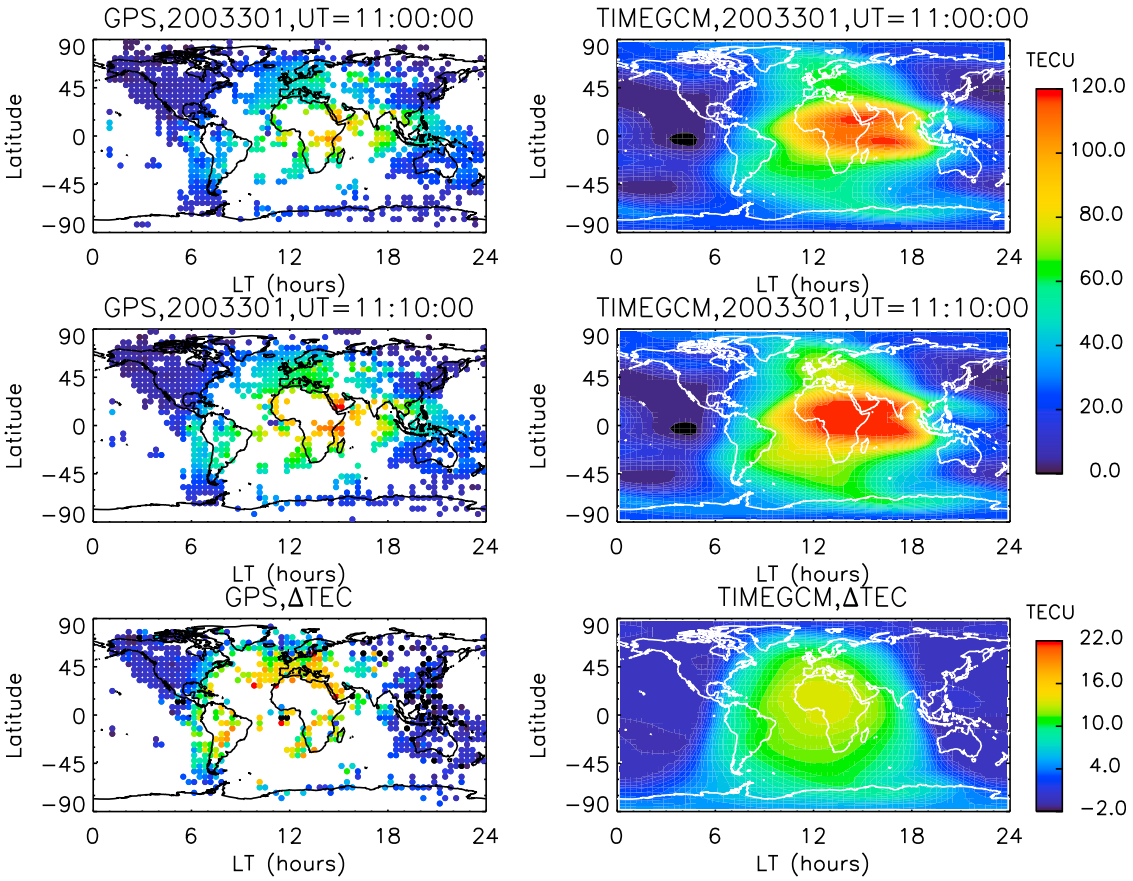

Figure 9. Comparisons of TEC observed by ground-based GPS network and TEC simulated by the TIME-GCM responding to the X17 near-center flare occurred on 28 October 2003. (left) GPS measurements of TEC for pre-flare, flare peak, and TEC enhancement. (right) TIME-GCM simulations of TEC for pre-flare, flare peak, and TEC enhancement. Pre-flare: ~1100 UT; flare peak: ~1110 UT. ΔTEC equals to TEC difference between 1110 and 1100 UT on 28 October 2003 minus TEC difference between 1110 and 1100 UT on 27 October 2003. FISM solar spectra were used as solar input for the TIME-GCM. 1 TEC unit is 10^{12} electrons/cm^2.

effect on temperature enhancement likely propagated to NO cooling and caused about 15% more NO cooling per unit mass at its peak altitude (~170 km) for the center flare. Space weather implications of solar flares, such as satellite drag, radio communications, as well as accuracy of the GPS, are related to neutral density in the upper thermosphere, electron density in the *F* region, and TEC. These parameters are determined by *F* region and upper thermosphere conditions where flare locations have large effects on I/T responses; therefore, flare location is an important factor in determining space weather consequences of flare effects.

[28] Ionospheric responses to the solar flares were nearly instant and there was no difference in the timing of peak responses between the center flare and the limb flare. Ion production reached a peak about 3 min after solar XUV and EUV radiation reached their peaks, and electron density then reached a peak about 25 min later. The main causes of the ionospheric disturbances were ion production and ion loss. Contributions by electron transport processes were relatively weak. The neutral atmosphere responded to enhanced heating due to enhanced ionization; neutral atmosphere properties, including temperature, composition, and neutral density, reached peaks more than 1 h after the electron density peak. Neutral dynamics then responded to neutral atmosphere heating; neutral wind disturbances were mainly in the day-night zonal direction; and the neutral wind peaked about 2.5 h later. This wind disturbance caused composition changes on a constant pressure surface that were much weaker and much more delayed than the composition changes at a constant altitude that were due to heating/expansion. Neutral temperature and composition disturbances then fed back to the ionosphere and caused some small and lagging disturbances in ion production, ion loss, and thus small electron density disturbance extending more than 1 day after the solar flares. Unlike their ionospheric counterparts, flare locations affected the timing of the peak responses of the neutral atmosphere, and neutral atmospheric responses to the limb flare peaked about 20 min later than those to the center flare.

[29] In this study, we assumed that two X17 flares occurred with the only difference between them being their locations on the solar disk and investigated the flare location effect on I/T responses and their space weather implications. The next step to advancing our understanding of solar flare effects on the terrestrial atmosphere is to investigate how the thermosphere and ionosphere respond to solar flares with

same locations and same intensities but with differences in other characteristics such as flare rising time and duration. Both data analysis and model studies will be needed for such investigations, and model-data comparisons can be made more extensive by including more flare events and more specific I/T phenomena that result from sudden increases of electron density, heating, and subsequent dynamical changes during a solar flare, such as traveling ionospheric disturbances and equatorial spread *F* in the post-sunset sector.

[30] **Acknowledgments.** The authors thank Anthea Coster for helping with the GPS TEC data. This research was supported by NASA grants NNX07AC61G, NNX08AQ31G, and NNX09AJ60G to the National Center for Atmospheric Research (NCAR), and by the Center for Integrated Space Weather Modeling (CISM). NCAR and CISM are supported by the National Science Foundation.

[31] Robert Lysak thanks Frederick Rich and another reviewer for their assistance in evaluating this paper.

References

Afraimovich, E. L., A. T. Altynsev, V. V. Grechnev, and L. A. Leonovich (2002), The response of the ionosphere to faint and bright solar flares as deduced from global GPS network data, *Ann. Geophys.*, *45*(1), 31–40.

Banks, P. M., and G. Kockarts (1973), *Aeronomy*, Academic Press, New York and London.

Chamberlin, P. C., T. N. Woods, and F. G. Eparvier (2007), Flare irradiance spectral model (FISM): Daily component algorithms and results, *Space Weather*, *5*, S07005, doi:10.1029/2007SW000316.

Chamberlin, P. C., T. N. Woods, and F. G. Eparvier (2008), Flare irradiance spectral model (FISM): Flare component algorithms and results, *Space Weather*, *6*, S05001, doi:10.1029/2007SW000372.

Coster, A., and A. Komjathy (2008), Space Weather and the Global Positioning System, *Space Weather*, *6*, S06D04, doi:10.1029/2008SW000400.

Davies, K. (1990), *Ionospheric Radio*, Peter Peregrinus, London.

Hagan, M. E., M. D. Burrage, J. M. Forbes, J. Hackney, W. J. Randel, and X. Zhang (1999), GSWM-98: Results for migrating solar tides, *J. Geophys. Res.*, *10*, 6813–6828.

Hedin, A. E. (1987), MSIS-86 thermosphere model, *J. Geophys. Res.*, *92*, 4649–4662.

Hedin, A. E. (1991), Extension of the MSIS thermosphere model into the middle and lower atmosphere, *J. Geophys. Res.*, *96*, 1159–1172.

Huba, J. D., H. P. Warren, G. Joyce, X. Pi, B. Iijima, and C. Coker (2005), Global response of the low-latitude to midlatitude ionosphere due to the Bastille Day flare, *Geophys. Res. Lett.*, *32*, L15103, doi:10.1029/2005GL023291.

Lindzen, R. S. (1981), Turbulence and stress owing to gravity wave and tidal breakdown, *J. Geophys. Res.*, *86*, 9707–9714.

Liu, J. Y., C. H. Lin, Y. I. Chen, Y. C. Lin, T. W. Fang, C. H. Chen, Y. C. Chen, and J. J. Hwang (2006), Solar flare signatures of the ionospheric GPS total electron content, *J. Geophys. Res.*, *111*, A05308, doi:10.1029/2005JA011306.

Meier, R. R., et al. (2002), Ionospheric and dayglow responses to the radiative phase of the Bastille Day flare, *Geophys. Res. Lett.*, *29*(10), 1461, doi:10.1029/2001GL013956.

Mendillo, M., et al. (1974), Behavior of the ionospheric F region during the great solar flare of August 7, 1972, *J. Geophys. Res.*, *79*, 665–672.

Mitra, A. P. (1974), *Ionospheric Effects of Solar Flares*, D. Reidel, Boston, Mass.

Mlynczak, M. G., et al. (2005), Energy transport in the thermosphere during the solar storms of April 2002, *J. Geophys. Res.*, *110*, A12S25, doi:10.1029/2005JA011141.

Picone, J. M., A. E. Hedin, D. P. Drob, and A. C. Aikin (2002), NRLMSISE-00 empirical model of the atmosphere: Statistical comparisons and scientific issues, *J. Geophys. Res.*, *107*(A12), 1468, doi:10.1029/2002JA009430.

Reigber, C., H. Lühr, and P. Schwintzer (2002), CHAMP mission status and perspectives, *Eos Trans. AGU*, *81*(48), F307.

Richards, P. G., J. A. Fennelly, and D. G. Torr (1994), EUVAC: A solar EUV flux model for aeronomic calculations, *J. Geophys. Res.*, *99*, 8981–8992.

Richmond, A. D., E. C. Ridley, and R. G. Roble (1992), A thermosphere/ionosphere general circulation model with coupled electrodynamics, *Geophys. Res. Lett.*, *19*, 601–604, doi:10.1029/92GL00401.

Rideout, W., and A. Coster (2006), Automated GPS processing for global total electron content data, *GPS Solut*, *10*, 219–228, doi:10.1007/s10291-006-0029-5.

Roble, R. G. (1995), Energetics of the mesosphere and thermosphere, in *The Upper Mesosphere and Lower Thermosphere: A Review of Experiment and Theory*, *Geophys. Monogr. Ser.*, vol. 87, edited by R. M. Johnson and T. L. Killeen, pp. 1–22, AGU, Washington, D. C.

Roble, R. G., and E. C. Ridley (1994), A thermosphere-ionosphere-mesosphere electrodynamics general circulation model (TIME-GCM): Equinox solar cycle minimum simulations (30–500 km), *Geophys. Res. Lett.*, *21*, 417–420.

Roble, R. G., E. C. Ridley, A. D. Richmond, and R. E. Dickinson (1988), A coupled thermosphere/ionosphere general circulation model, *Geophys. Res. Lett.*, *15*, 1325–1328.

Solomon, S. C., and L. Qian (2005), Solar extreme-ultraviolet irradiance for general circulation models, *J. Geophys. Res.*, *110*, A10306, doi:10.1029/2005JA011160.

Strickland, D. J., et al. (2007), Constraining and validating the Oct/Nov 2003 X class EUV flare enhancements with observations of FUV dayglow and *E* region electron densities, *J. Geophys. Res.*, *112*, A06313, doi:10.1029/2006JA012074.

Sutton, E. K., J. M. Forbes, and R. S. Nerem (2005), Global thermospheric neutral density and wind response to the severe 2003 geomagnetic storms from CHAMP accelerometer data, *J. Geophys. Res.*, *110*, A09S40, doi:10.1029/2004JA010985.

Sutton, E. K., J. M. Forbes, R. S. Nerem, and T. N. Woods (2006), Neutral density response to the solar flares of October and November, 2003, *Geophys. Res. Lett.*, *33*, L22101, doi:10.1029/2006GL027737.

Tsurutani, B. T., et al. (2005), The October 28, 2003 extreme EUV solar flare and resultant extreme ionospheric effects: Comparison to other Halloween events and the Bastille Day event, *Geophys. Res. Lett.*, *32*, L03S09, doi:10.1029/2004GL021475.

Tsurutani, B. T., et al. (2006), Extreme solar EUV flares and ICMEs and resultant extreme ionospheric effects: Comparison of the Halloween 2003 and the Bastille Day events, *Radio Sci.*, *41*, RS5S07, doi:10.1029/2005RS003331.

Woods, T. N., F. G. Eparvier, S. M. Bailey, P. C. Chamberlain, J. Lean, G. J. Rottman, S. C. Solomon, W. K. Tobiska, and D. Woodraska (2005), The Solar EUV Experiment (SEE): Mission overview and first results, *J. Geophys. Res.*, *110*, A01312, doi:10.1029/2004JA010765.

Woods, T. N., et al. (2008), XUV photometer system (XPS): Improved solar irradiance algorithm using CHIANTI spectral models, *Solar Phys.*, *250*, 235–267, doi:10.1007/s11207-008-9196-6.

Worden, J. R., T. N. Woods, and K. W. Bowman (2001), Far-ultraviolet intensities and center-to-limb variations of active regions and quiet Sun using UARS SOLSTICE irradiance measurements and ground-based spectroheliograms, *Astrophys. J.*, *560*, 1020, doi:10.1086/323058.

Zhang, D. H., Z. Xiao, and Q. Zhang (2002), The correlation of flare's location on solar disc and the sudden increase of total electron content, *Chin. Sci. Bull.*, *47*, 82–85, doi:10.1360/02tb9017.

A. G. Burns, L. Qian, and S. C. Solomon, High-Altitude Observatory, National Center for Atmospheric Research, Boulder, CO 80301, USA. (lqian@ucar.edu)

P. C. Chamberlin, Solar Physics Laboratory, NASA Goddard Space Flight Center, Code 671, Greenbelt, MD 20771, USA.